Spin torque effect on topological defects and transitions of magnetic domain phases in Ta/CoFeB/MgO

Kang Wang, Lijuan Qian, Wenzhe Chen, See-Chen Ying, Gang Xiao, and Xiaoshan Wu

Phys. Rev. B **99**, 184410 — Published 10 May 2019

DOI: 10.1103/PhysRevB.99.184410

Spin torque effect on topological defects and transitions of magnetic domain phases in Ta/CoFeB/MgO

Kang Wang,[1,2] Lijuan Qian,[2] Wenzhe Chen,[2] See-Chen Ying,[2*] Gang Xiao,[2,†] Xiaoshan Wu[1,‡]

[1]*Collaborative Innovation Center of Advanced Microstructures, Laboratory of Solid State Microstructures, School of Physics, Nanjing University, Nanjing 210093, China*

[2]*Department of Physics, Brown University, Providence, Rhode Island 02912, USA*

Abstract

Using the polar magneto optical Kerr effect microscope, we have observed in a prototypical multilayer system of Ta/CoFeB/MgO a spin current-driven transformation of an initial labyrinthine domain pattern. The labyrinthine domain phase can either transform into a dense array of skyrmions, or simply has a change in the orientational order, depending on the strengths of the applied spin current pulse and the external magnetic field. We conclude both from experimental studies and micromagnetic simulations that the applied spin current leads to the generation/deletion of topological defects through modifying the motion of domain walls and the magnetic configurations within the domain walls, leading to the observed transformations. This is different from the thermally-induced transitions where the nucleation and proliferation of topological defects are the dominant factors.

* see-chen_ying@brown.edu
† gang_xiao@brown.edu
‡ xswu@nju.edu.cn

Exchange interactions between two atoms of a ferromagnetic layer can be mediated by a third nonmagnetic atom with large spin-orbit coupling, leading to the Dzyaloshinskii-Moriya interaction (DMI). The DMI created at the interface between a ferromagnetic layer and a heavy-metal layer decreases the domain wall energy density and increases domain period of magnetic domain structures that are stabilized by competing interactions including dipole interactions and anisotropy, etc. The phase diagrams of magnetic domain structures have been discovered in multiple prototypical multilayer systems [1-5]. In the vicinity of the spin reorientation transition from the perpendicular magnetization to in-plane magnetization, labyrinthine phases appear [1,5,6]. The positional and orientational orders of labyrinthine domain patterns, as well as the domain width, greatly depend on the anisotropy and external parameters such as temperature [4,7-9]. It has been proposed and demonstrated that nucleation and proliferation of topological defects play important roles in thermally induced transitions between diverse labyrinthine domain phases [6-8]. The topological defects, as schematically presented in Fig. 1, include the unbound defects (such as concave disclination, three segments meeting at one point (A-type or B-type, with reversed magnetization)) and bound defects (such as magnetic domain with the "H"-shape (C-type) that constitutes of two unbound defects, and the domain surrounding a magnetic bubble (D-type)). Studies on thermal effects on fluctuations of different types of topological excitations confirm that the unbound defects are predominant in domain pattern transformations, and the bound defects show reduced fluctuations [6]. The topological defects-related transformations of labyrinthine domain present analogues to phase transitions in other quasi two-dimensional systems such as transitions between nematic and smectic phases in liquid crystal systems [8,10,11].

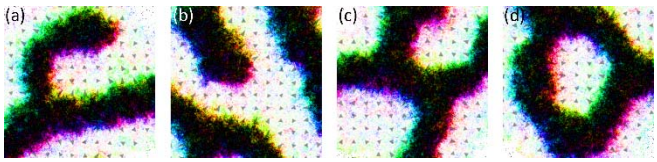

FIG. 1. Schematic presentations of topological defects. (a) A-type defect formed by three segments of downward domains meeting at one point. (b) B-type defect formed by three segments of upward domains meeting at

one point. (c) C-type defect that constitutes of two A-type defects. (d) D-type defect formed by domain surrounding a magnetic bubble. The white and black contracts refer to upward and downward magnetization, respectively.

The labyrinthine domain pattern can undergo a transition into individual skyrmions with increasing perpendicular magnetic field [1,5]. The topologically stabilized magnetic skyrmions exhibit fascinating behaviors such as high-speed motion driven by an applied spin current with much lower current density than the current density required for driving magnetic domain walls [3,12]. This promises that skyrmions have great potential in applications of the next-generation of spintronic devices with lower energy-consumptions [13-15]. The critical magnetic field H_c, above which the labyrinthine multi-domain transforms into skyrmions, depends greatly on magnetic parameters, especially the competition between the DMI and Heisenberg exchange interactions of systems [1,5,16]. The critical field for the transition can be reduced by approximately a factor of two with the application of a spin current pulse [16]. Micromagnetic simulations reveal that topological defects responding to the spin current are important in the current-dependent transitions into skyrmions [17]. However, the dynamics of topological defects interacting with the spin current, and their influences on multiple domain phases, so far have rarely been studied.

For the present study, we focus on the spin torque effect on topological defects and transitions of magnetic domain phases in a prototypical multilayer stack of Ta/CoFeB/MgO. To reveal the microscopic nature of current-driven transitions, we use the technique of polar Magneto Optical Kerr effect (P-MOKE) microscope, complemented by micromagnetic simulations studies.

The multilayer stacks of Ta(6.0)/CoFeB(1.0)/MgO(1.6)/Ta(1.0) as presented in Fig. 2(a) were deposited on thermally oxidized silicon wafers using high vacuum magnetron sputtering. Numbers in the brackets are layer thicknesses in nanometer (nm), and CoFeB refers to the ferromagnetic alloy $Co_{40}Fe_{40}B_{20}$. Hall bar structures with 140 μm long and 20 μm wide stripes were patterned using the photo lithography and ion milling [18]. With the Hall bar structure, we can apply the charge current along the

long axis of the stripe and detect the Hall resistance of samples through the leads with the width of 5 μm. The bottom Ta(6.0) layer acts as a platform to transfer the charge current ($\boldsymbol{J}_{\mathrm{e}} = J_{\mathrm{e}}\boldsymbol{e}_{\mathrm{x}}$) to spin current ($\boldsymbol{J}_{\mathrm{s}} = J_{\mathrm{s}}\boldsymbol{e}_{\mathrm{z}}$) (Fig. 1(b), $\boldsymbol{e}_i$ is the unit vector along the i-axis (i = x, y, or z)). The spin current with the in-plane spin polarization ($\boldsymbol{m}_{\mathrm{p}} = \frac{\boldsymbol{e}_{\mathrm{z}} \times \boldsymbol{J}_{\mathrm{e}}}{|\boldsymbol{J}_{\mathrm{e}}|}$) exerts spin torques on magnetizations in the ferromagnetic layer, resulting in manipulations of magnetic domains. The charge-to-spin current conversion results from the large spin-orbit coupling of Ta atoms [19,20]. This is known as the spin Hall effect characterized by the spin Hall angle $|\Theta_{\mathrm{SH}}| = \frac{J_{\mathrm{s}}}{J_{\mathrm{e}}}$ that has a value of about 0.14 for Ta [21]. The MgO layer, in which the p electronic states of oxygen atoms are hybridized with the d electrons of the ferromagnetic atoms in the adjacent CoFeB layer, enhances the perpendicular magnetic anisotropy [22]. Thermally annealing the sample in a moderate condition which manipulates the interface is generally employed to introduce the desired magnetic structures [21,22]. The top Ta(1.0) layer is partially oxidized on exposure to the atmosphere which prevents the underlying layers from further oxidization.

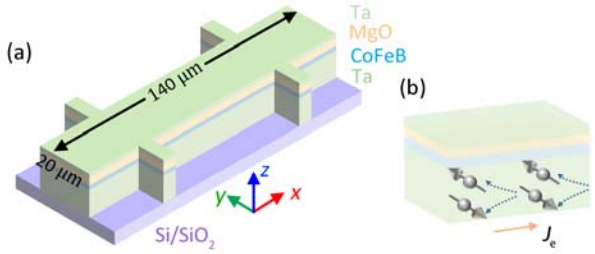

FIG. 2. (a) The schematic depiction of the magnetic stack of Si/SiO_2/Ta(6.0)/CoFeB(1.0)/MgO(1.6)/Ta(1.0) with a Hall bar structure. (b) Sketch of the conversion of the charge current to spin-polarized current in the bottom Ta(6.0) layer.

We anneal samples in a high vacuum chamber (~10^{-6} Torr) at a temperature of 210 ˚C for one hour and cool down samples naturally while applying a perpendicular magnetic field of ~0.42 T. The resulting magnetic property of the multilayer and magnetic field-dependent magnetic configurations are shown in Fig. 3. At zero external magnetic field, the Hall resistance (R_{H}) measurement (Red circle in Fig.

3(a)) indicates an absence of the remnant magnetization. It is consistent with the magnetization measurement and the observed labyrinthine multi-domain state recorded by the P-MOKE microscope (Fig. 3(b)). The bright and dark contrasts in P-MOKE images, respectively, correspond to upward ($+M_z$) and downward ($-M_z$) out-of-plane magnetization. We highlight A-, B-, C- and D-type topological defects that are defined previously by coloring $+M_z$ domain and $-M_z$ domain in yellow and orange, respectively. With increasing magnetic field (H_z) along the +z-direction, the $+M_z$ domains overspread and $-M_z$ domains shrink into the mixed skyrmion and labyrinthine domain phase (Fig. 3(c) with $H_z = 11$ Oe). The mixed phase is followed by the state with multiple magnetic skyrmions (Fig. 3(d) with $H_z = 22$ Oe) and finally uniform magnetization state at even higher magnetic fields. We confirm that the magnetic bubbles presented in Fig. 3(d) are topologically stabilized skyrmions (Fig. 3(e)), from current-driven skyrmion motion where we observe skyrmion Hall effect through the gyrotropic motion of skyrmions [23]. The left-handed Néel-component of magnetic domain walls is evidenced by the asymmetric expansion of magnetic domains along the direction of an in-plane magnetic field [23], while Bloch-type domain walls would expand perpendicularly to the in-plane field and domain walls with opposite vorticities would also expand conversely [24].

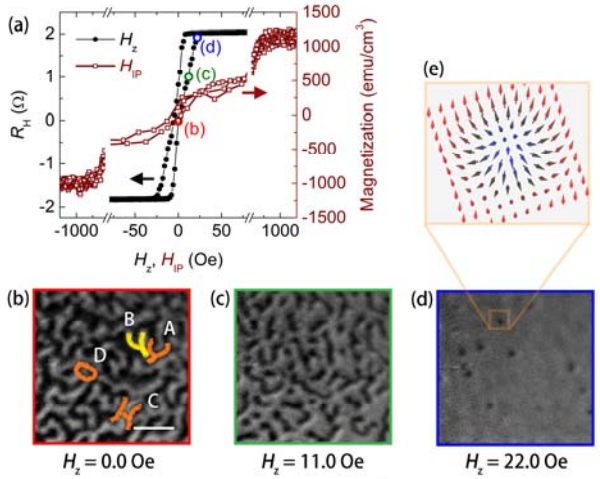

FIG. 3. (a) Hall resistance (R_H) with perpendicular magnetic field (H_z), and the magnetization curve with in-plane magnetic field (H_{IP}). The high and low Hall resistance correspond to the uniform states with upward ($+M_z$) and downward ($-M_z$) out-of-plane magnetization, respectively. (b)-(d) A series of P-MOKE images acquired in the

presence of a perpendicular magnetic field, gradually increasing from a negative saturation magnetic field to 0.0 Oe (b), 11.0 Oe (c) and 22.0 Oe (d). These magnetic states give rise to the anomalous Hall resistance as presented in (a), highlighted by circles in same colors of corresponding squares in (b)-(d). The white line in (b) is with the length of 5 μm. The A-, B-, C- and D-type topological defects presented in (b) are highlighted by coloring upward and downward domain in yellow and orange, respectively. (e) The schematic presentation of a skyrmion.

It has been demonstrated that the topological charge density $q(\boldsymbol{r}) = \boldsymbol{m} \cdot \left(\partial_{\mathrm{x}}\boldsymbol{m} \times \partial_{\mathrm{y}}\boldsymbol{m}\right)/4\pi$ of a magnetic texture, where $\boldsymbol{m} = \left(m_{\mathrm{x}}, m_{\mathrm{y}}, m_{\mathrm{z}}\right)$ is the normalized magnetization, determines its dynamics in responses to the spin current [17,25,26]. In addition to skyrmions, half-skyrmions at the ends of a stripe domain, as well as topological defects observed in multiple domain phases as presented in Fig. 3(b), have non-zero distributions of topological charge densities [6,7,10]. Their responses to spin current, and contributions to transformations of magnetic domain phases, are the main focus of this work.

Figure 4 shows the current- and pulse repetitions-dependent magnetic configurations in a field-free environment. Before applying current pulses, disordered magnetic configurations are recorded (Figs. 4(a), (d) and (g)). The absence of the orientational and positional order of the domain pattern is due to the lack of crystallographic orientations in the ferromagnetic layer. Applications of current pulses lead the labyrinthine domain to transform into an oriented state. The orientational order increases first and then however decreases with increasing the magnitude of current pulses (Figs. 4(c), (f) and (i)). We quantify the orientational order of a labyrinthine domain phase from the two-dimensional fast Fourier transformation (2D-FFT) of the domain pattern (Fig. 4(j)) [23]. For a labyrinthine domain with a strong orientation order, the peak position φ_{p} (marked by the black arrow in Fig. 4(k)) of the angular distributions of 2D-FFT intensities is closer to π and the full width half maximum $\Delta\varphi_{\mathrm{FWHM}}$ gets smaller than the $\Delta\varphi_{\mathrm{FWHM}}$ of a weakly-oriented magnetic domain phase. Current-dependences of φ_{p} and $\Delta\varphi_{\mathrm{FWHM}}$ confirm that the maximal orientational order occurs at an applied current ranging from 8 mA to 15 mA (Fig. 4(l)).

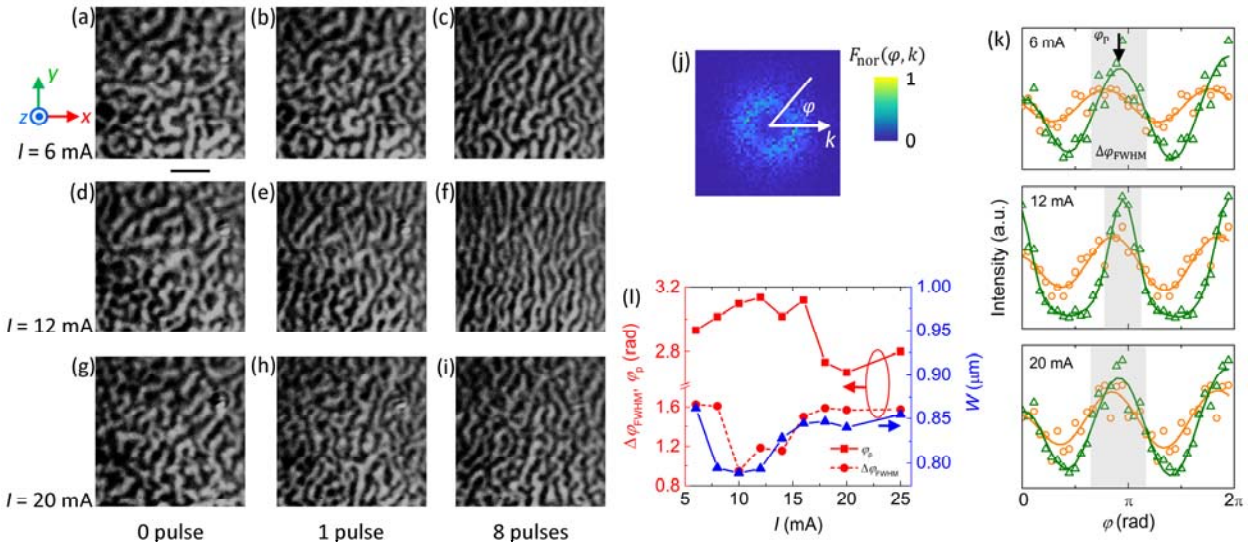

FIG. 4. (a)-(c) P-MOKE images recorded before applying current pulses (a), after applying one current pulse (b) and eight current pulses (c), with the current of 6 mA at zero magnetic field. (d)-(f) P-MOKE images recorded before applying current pulses (d), after applying one current pulse (e) and eight current pulses (f), with the current of 12 mA. (g)-(i) P-MOKE images recorded before applying current pulses (g), after applying one current pulse (h) and eight current pulses (i), with the current of 20 mA. The black line in (a) is with the length of 5 μm. The current flowing in the bottom Ta layer is along *x*-axis. (j) The two-dimensional fast Fourier transformation (2D-FFT) of the magnetic domain pattern recorded at a zero magnetic field. The color bar represents the normalized 2D-FFT intensities $F_{\mathrm{nor}}(\varphi, k)$ as functions of the radial (k) and angular (φ) coordinates. (k) Angular distributions of 2D-FFT intensities of domain patterns before (orange dots and lines) and after (green dots and lines) applying current pulses with different current values. Dots are experimental data and lines are guides to the eye [23]. (l) Current-dependences of φ_{p}, $\Delta\varphi_{\mathrm{FWHM}}$ and domain width W.

We evaluate the domain width W through the angular integrations of the 2D-FFT intensities of the magnetic domain pattern (Fig. 4(l)) [23]. The width W varies inversely as the orientational order. It has been revealed through an elastic continuum model that the domain width is greatly related to the number of topological defects [9]. This suggests that transformations of magnetic configurations presented in Fig. 4 are possible to originate from the topological defects interacting with the driving current.

To follow the current-induced transformations in detail and reveal the effects of topological defects in transformation processes, we image magnetic patterns after applying each current pulse with the current of 12 mA and 20 mA (Fig. 5). The first two current pulses influence domain patterns greatly, during applications of which it is hard to track variations of magnetic configurations exactly. However, magnetic domains tend to be aligned along the *y*-axis, and some topological defects such as the B-type defect that is marked by yellow lines in Fig. 5(c) are observed, after applying two current pulses with the current of 12 mA. The topological defect with upward magnetization disconnects downward domains (purple lines in Fig. 5(c)), corresponding to a weakly ordered domain phase. Application of the third current pulse leads the disconnected downward domains to interconnect to form the A-type defect (purple lines in Fig. 5(d)) that is a reversion in magnetization of the B-type defect. The A-type defect further transforms into the C-type one with the "H"-shape (Fig. 5(e)), with the application of an additional current pulse. Finally, the current leads to the merging of upward domains and the deletion of the topological defect (Fig. 5(f)). Both upward and downward stripes without obvious topological excitations emerge (Fig. 5(f)), resulting in an ordered domain phase.

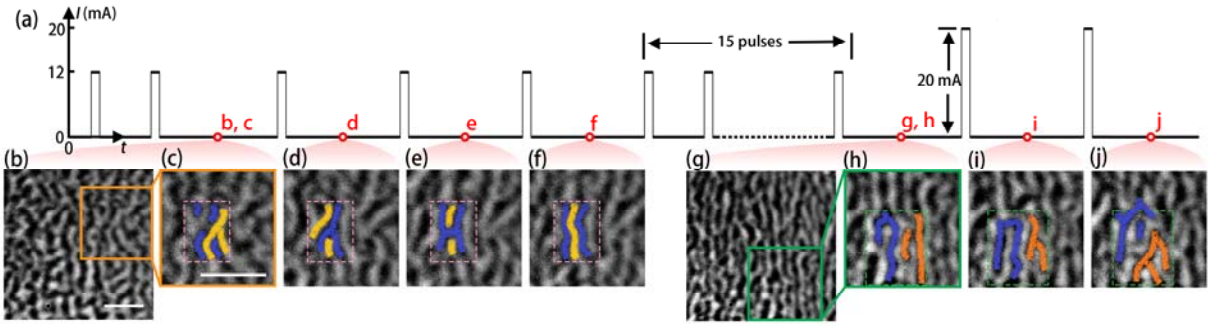

FIG. 5. The effects of topological defects on current-driven transitions of labyrinthine domain phases. We first increase magnetic field from the negative saturation magnetic field to a zero field, before applying current pulses. P-MOKE images with modifications by current pulses are recorded in a field-free environment. (a) The schematic depiction of current pulses applied, with the pulse width of 50 μs. (b) The magnetic configuration recorded after applying two current pulses with the current of 12 mA. (c) The enlarged image of the area in the orange square in (a). (d)-(f) P-MOKE images recorded after applying three (d), four (e) and five pulses (f), with the

current of 12 mA. Purple lines represent the $-M_z$ domain, and yellow lines represent the $+M_z$ domain. (g) The P-MOKE image recorded after applying twenty current pulses with the current of 12 mA which leads to a state with a strong orientational order. (h) The enlarged image of the area in the green square in (g). (i)-(j) Magnetic states that are transformed from (h) with applying one (i) and two current pulses (j) with the current of 20 mA. The purple and orange lines both represent the $-M_z$ domain in two separate areas. Lines in (b) and (c) are both with the length of 5 μm. The current flowing in the bottom Ta layer is along the *x*-axis.

In contrast to the current-induced deletion of topological defects as presented in Figs. 5(b)-(f), applications of current pulses with a larger current of 20 mA generate topological defects in the domain pattern (Figs. 5(g)-(j)). This leads the domain pattern to transform into a configuration with a weaker orientational order. We attribute the generation of topological defects to the combined effect of the breaking and merging of magnetic domains when applying a large current. Both the current-induced motion of topological defects and presence of pinning sites in multilayer stacks possibly induce domain patterns to be cut by the spin current. This is also the reason for the transformation of labyrinthine domains into skyrmions, which we present next, at a moderate magnetic field.

Figure 6 shows the magnetic configurations manipulated by an applied current pulse of 20mA at $H_z = 8.0$ Oe and 16.0 Oe. Clearly, the presence of an external magnetic field and a large current pulse results in a final state of a dense array of magnetic skyrmions. It has been proposed on basis of micromagnetic simulations that the spin current moves half-skyrmions at the ends of the stripe [17]. The motion of half-skyrmions leads to the bending of the stripe and produce more defects. The motion of topological defects with non-zero topological charge densities ultimately pinches off the stripe into a dense array of skyrmions, corresponding to what we observe experimentally as shown in Figs. 6(d) and (g). Similar phenomena have also been observed in Pt/Co/Ta multilayers; there a much higher magnetic field ($H_z = 270$ Oe) is needed to dynamically generate skyrmions [16]. In Pt/Co/Ta multilayers, the skyrmion size is smaller and stability of skyrmions is higher. From the aspect of energy consumption, the great decrease in the critical magnetic field for the system studied in our work is desirable for future skyrmion-based applications.

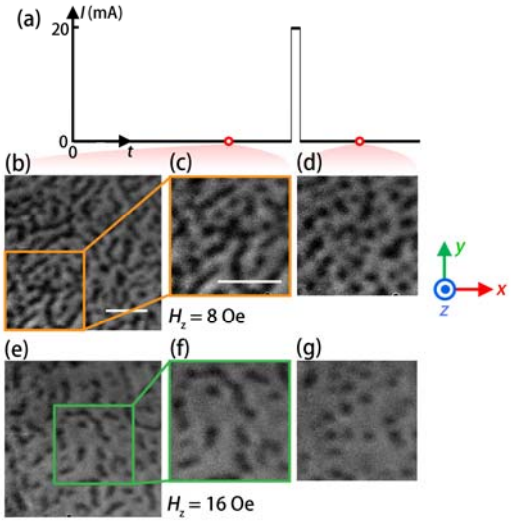

FIG. 6. (a) The schematic depiction of current pulses applied, with the pulse width of 50 μs, and the current of 20 mA. (b) The P-MOKE image recorded at the magnetic field of 8 Oe. (c) The enlarged image of the area in the orange square in (b). (d) The P-MOKE image recorded in the same area shown in (c) after applying a current pulse at the magnetic field of 8 Oe. (e) The P-MOKE image recorded at the magnetic field of 16 Oe. (f) The enlarged image of the area in the green square in (e). (g) The P-MOKE image recorded in the same area shown in (f) after applying a current pulse at the magnetic field of 16 Oe. Lines in (b) and (c) are both with the length of 5 μm. The charge current flowing in the bottom Ta(6.0) layer is along the *x*-axis.

We summarize the resulting magnetic configurations after applying current pulses at different magnetic fields in a phase diagram as presented in Fig. 7. Results show that the critical field H_c above which skyrmions state appears decreases with increasing the current, and saturates at about 8 Oe when the current is above $I_c = 15$ mA. The current I_c is close to the value beyond which the orientational order starts to decrease at zero magnetic field (Fig. 4(l)). This correlation leads us to believe that the breaking of magnetic domains plays an important role in the transformation into an array of skyrmions or a weakly-oriented state when applying a large current, while the merging of magnetic domains is predominant with applications of a small current leading to the deletion of topological defects.

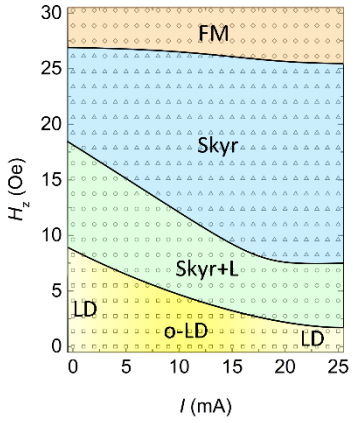

FIG. 7. The phase diagram of the multilayer stack of Ta/CoFeB/MgO as a function of applied current pulse and external magnetic field. The magnetic domain phases are identified through P-MOKE microscope after applying the current at different perpendicular magnetic fields . Labyrinthine domain phases with a weak (LD) and a strong (o-LD) orientational order, a mixed skyrmion and labyrinthine domain phase (Skyr+L), the magnetic skyrmion state (Skyr) and the uniform magnetic phase (FM) are identified. Lines are guides to the eye.

To gain a better microscopic understanding of magnetic domains responding to the spin current, especially the merging of magnetic domains as a response to the spin torque, we have performed micromagnetic simulations studies for our system using finite-difference solver MUMAX3 based on the graphic processor unit (GPU) [27]. In the micromagnetic simulations studies, the spin torque comes from the functional derivative of the free energy including exchange, anisotropy, DMI and dipolar energy terms, as well as a Slonczewski STT due to the influx of spin current [28]. The time-dependent normalized magnetization is obtained from solving the Landau-Lifshitz-Gilbert (LLG) equation. The magnetic parameters we adopt for the simulations studies are saturation magnetization , perpendicular magnetic anisotropy and Gilbert damping coefficient . The value of is obtained from the in-plane and out-of-plane hysteresis loops measured by the vibrating-sample magnetometer (Fig. 3(a) where the out-of-plane hysteresis loop is not shown). The area between the out-of-plane and in-plane hysteresis loops is used to determine the effective magnetic anisotropy which provides the perpendicular magnetic anisotropy . The value of

is taken from the experimental result in literatures [29]. We also take thermal fluctuations with the temperature of 300 K into simulations by adding a stochastic thermal field into the LLG equation [27,30], in order to achieve results comparable with the experimental data.

There are uncertainties about the proper values to use for the exchange stiffness and DMI constant for the present system. In the CoFeB layer, the exchange stiffness may vary by a factor of two, depending on annealing temperature and the ferromagnetic layer thickness [29,31]. We have performed simulations adopting different values of while keeping and , respectively. The domain width of the relaxed magnetic configuration from the random magnetization state increases with decreasing (Fig. 8(b)). Extrapolation of the trend of versus gives for , and for , to obtain the labyrinthine domain phase with the same domain width as experimental observations. The values are close to the DMI constant reported previously in similar systems [32]. It has been shown that chirality of magnetic domain walls depends on relative values of and . When , the domain walls belong to the mixed Bloch and Néel-types, and the domain walls become purely Néel-type when . We calculate the dependence of on exchange stiffness (Fig. 8(a)), with the given , and . The fact that suggests the purely Néel-type domain walls, consistent with the experimental evidences [23].

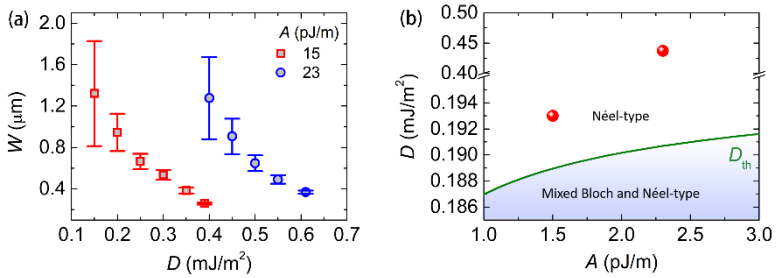

FIG. 8. (a) Domain widths of the relaxed magnetic configuration in simulations, as a function of the DMI constant , with adopting (red square dots) and (blue circle dots). (b) Dependence

of the D_{thr} on A (green line). Red dots are derived from (a) to obtain the labyrinthine domain phase with the same domain width as experimental observations.

In the following, we perform simulations on the basis of the relaxed magnetic configuration from a random magnetization state in a $8 \times 8\ \mu\mathrm{m}^2$ effective ferromagnetic layer from the simulation study, with adopting $D = 0.193 \times 10^{-3}\ \mathrm{J/m^2}$ and $A = 1.5 \times 10^{-11}\ \mathrm{J/m}$, as shown in Fig. 9(a), to give a general picture for spin torque effect on topological defects and transition of magnetic domain phases. The ferromagnetic layer is discretized into cells of $4\ \mathrm{nm} \times 4\ \mathrm{nm} \times 1\mathrm{nm}$. These dimensions are smaller than the exchange length $l_{\mathrm{ex}} = \sqrt{A/\left(\frac{1}{2}\mu_0 M_{\mathrm{S}}^2\right)} = 4.61\ \mathrm{nm}$, ensuring numerical accuracy. The underlying mechanisms including both current-driven motion of topological defects and rotation of magnetization within domain walls are similar for the variable ranges of DMI constant and exchange stiffness because of the nature of Néel-type magnetic domain walls.

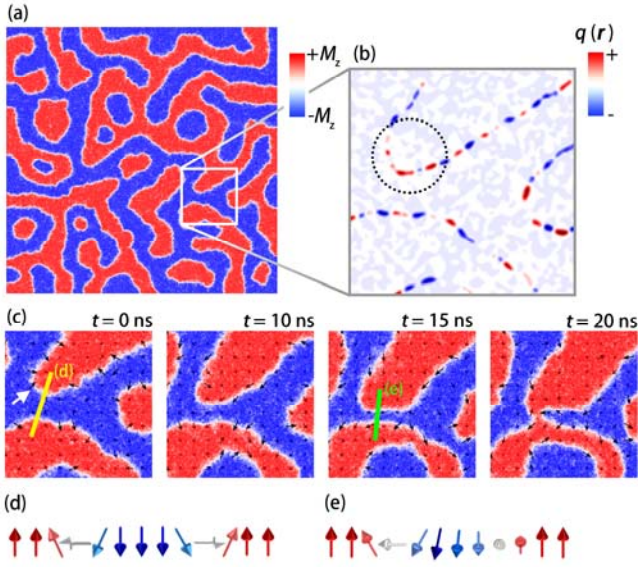

FIG. 9. Micromagnetic simulation results showing the merging of magnetic domains due to the spin torque. (a) The initial magnetic configuration relaxed from a random magnetization at a zero magnetic field. The size of the image is $8 \times 8\ \mu\mathrm{m}^2$. (b) Spatial distributions of topological charge densities ($q(\boldsymbol{r})$) of the magnetic domain phase presented in the white square in (a). (c) Time dependent spin current-driven variations of magnetic configurations in

the white square shown in (a). The black dotted circle in (b) and the white arrow in (c) is used to mark the position of the endcap of the $+M_z$ domain. (d) A schematic diagram of magnetizations along the yellow line in (c). (e) A schematic diagram of magnetizations along the green line in (c).

The spatial distribution of topological charge densities of the relaxed magnetic configuration is presented in Fig. 9(b). We apply the current with the spin current density of $J_s = 1.4 \times 10^9$ A/m^2 and the spin polarization pointing to $-\boldsymbol{e}_y$ to the initial state shown in Fig. 9(a). It corresponds to an effective application of charge current $\boldsymbol{J}_e = J_e \boldsymbol{e}_x$ with $J_e = -\frac{J_s}{|\Theta_{SH}|} = -1.0 \times 10^{10}$ A/m^2 in the adjacent Ta layer. Taking into calculations the resistivity ($\rho_{Ta} \approx 200\ \mu\Omega$ cm) of the Ta layer and the resistivity ($\rho_{CoFeB} \approx 100\ \mu\Omega$ cm) of the CoFeB layer, which are extracted from our previous studies [21], the effective application of the current in the bottom Ta layer is estimated about 1.80 mA which possibly result in the transformation into a weakly-oriented magnetic configuration.

Applications of the spin current exert both the field-like torque $\boldsymbol{\tau}_{FL} = -\beta J_e \frac{\epsilon' - \alpha\epsilon}{1+\alpha^2} \boldsymbol{m} \times \boldsymbol{m}_p$ and damping-like torque $\boldsymbol{\tau}_{DL} = \beta J_e \frac{\epsilon - \alpha\epsilon'}{1+\alpha^2} \left(\boldsymbol{m} \times \left(\boldsymbol{m}_p \times \boldsymbol{m} \right) \right)$ on magnetizations in the ferromagnetic layer [27]. In expressions for $\boldsymbol{\tau}_{FL}$ and $\boldsymbol{\tau}_{DL}$, $\beta = \frac{|\Theta_{SH}|\hbar}{M_S e d}$ where $\hbar$ and e are reduced Plank's constant and elementary electronic charge, respectively, and $\epsilon = \frac{P\Lambda^2}{(\Lambda^2+1)+(\Lambda^2-1)(\boldsymbol{m}\cdot\boldsymbol{m}_p)}$ where P is the spin polarization of the spin current. ϵ' determines the amplitude of the $\boldsymbol{\tau}_{FL}$ relative to $\boldsymbol{\tau}_{DL}$. We set $\Lambda = 1$ to remove the dependence of ϵ on $\boldsymbol{m} \cdot \boldsymbol{m}_p$, and set $P = 1$ and $\epsilon' = 1$ to adjust the coefficient of $\boldsymbol{\tau}_{FL}$ to the same as the coefficient of $\boldsymbol{\tau}_{DL}$. We choose these parameters according to the recent harmonic Hall measurements for a Ta/ferromagnetic system that the coefficients of $\boldsymbol{\tau}_{FL}$ and $\boldsymbol{\tau}_{DL}$ have the similar values [33].

Modified profiles by the spin current at different delay times are presented in Fig. 9(c). Here we take variations of the domain pattern in the white square in Fig. 9(a) as an example. A rounded endcap of the $+M_z$ domain (pointed by the white arrow in Fig. 9(c)) moves along the current-driven force with an

additional transverse motion along the -*y*-direction. The current-driven transverse motion of the endcap elongates the $+M_{\mathrm{z}}$ domain, leading the magnetic domain to be aligned along the *y*-axis. If we consider the endcap as a rigid half skyrmion, the transverse motion of the half skyrmion can be qualitatively described through the derived Thiele equation [17,25,26]

$$\boldsymbol{\mathcal{G}} \times \boldsymbol{v} + \alpha \mathcal{D} \boldsymbol{v} + \frac{1}{2}\gamma\beta \boldsymbol{\mathcal{T}} = 0, \tag{1}$$

which is initially used to describe skyrmion motion as responses to the spin current. The first term and the second term as functions of the velocity vector $\boldsymbol{v} = (\boldsymbol{v}_{\mathrm{x}}, \boldsymbol{v}_{\mathrm{y}}, \boldsymbol{v}_{\mathrm{z}})$ of the magnetic texture are known as Magnus force and dissipative force, respectively. The gyro coupling vector $\boldsymbol{G}$ only has a *z*-component $\mathcal{G} = 4\pi \int q(\boldsymbol{r}) dxdy$ which is an integration of the topological charge density $q(\boldsymbol{r})$ that is non-zero at domain walls. $\mathcal{D}$ is the dissipative parameter that is calculated to be about 19.3373 for a rigid half-skyrmion mass. The third term is the current-induced driving force for the motion of a magnetic texture, with the coefficient $\frac{1}{2}\gamma\beta = \frac{\gamma|\Theta_{\mathrm{SH}}|\hbar}{2M_{\mathrm{S}}ed}$ and the vector $\boldsymbol{\mathcal{T}} = \int (\boldsymbol{e}_{\mathrm{z}} \times \boldsymbol{J}_{\mathrm{e}}) \cdot (\boldsymbol{\nabla m} \times \boldsymbol{m}) dxdy$, where γ is the gyromagnetic ratio. For a rigid half-skyrmion, $\boldsymbol{\mathcal{T}} = \frac{\pi^2}{2} R_{\mathrm{h-sky}} \overleftrightarrow{\boldsymbol{\Gamma}} (\boldsymbol{e}_{\mathrm{z}} \times \boldsymbol{J}_{\mathrm{e}})$ with the tensor $\overleftrightarrow{\boldsymbol{\Gamma}} = \begin{bmatrix} 0 & -1 & 0 \\ 1 & 0 & 0 \\ 0 & 0 & 0 \end{bmatrix}$, and $R_{\mathrm{h-sky}}$ is the radius of the half-skyrmion mass. The Equation (1) used to describe the current-driven skyrmions motion is with same parameters of $\mathcal{D}$ and β, but with a different $\mathcal{G}$ which equals $+4\pi$ or -4π for a rigid skyrmion mass. We note, from derivation processes for the Thiele equation [26], that even a small segment of the magnetic domain, which can be considered as a small part of a skyrmion, can also be qualitatively described by the Equation (1). However, in this scenario, the second term of Equation (1) is universally rewritten as $\alpha \overleftrightarrow{\boldsymbol{\mathcal{D}}} \boldsymbol{v}$ with the component of the tensor $\overleftrightarrow{\boldsymbol{\mathcal{D}}}$ calculated to be $\mathcal{D}_{ij} = \int (\partial_i \boldsymbol{m} \cdot \partial_j \boldsymbol{m}) dxdy$ $(i, j = x \text{ or } y)$.

It is suggested from Fig. 9(b) that there are dispersed distributions of topological charge densities near domain walls. The dispersion in topological charge densities is attributed to thermal fluctuations. However, the sign of an integration of topological charge densities of a magnetic texture is only related to

the magnetic configuration and independent of the temperature. An integration of $q(\boldsymbol{r})$ of the endcap (marked by the black dotted circle in Fig. 9(b)) leads to a positive value of $\mathcal{G}$. We decompose the Equation (1) into two normal components,

$$-\mathcal{G}v_{\mathrm{y}} + \alpha\mathcal{D}v_{\mathrm{x}} - \frac{\pi^2}{4}R_{\mathrm{h-skyr}}\gamma\beta J_{\mathrm{e}} = 0, \tag{2}$$

$$\mathcal{G}v_{\mathrm{x}} + \alpha\mathcal{D}v_{\mathrm{y}} = 0. \tag{3}$$

The transverse velocity of the endcap is calculated to be $v_{\mathrm{y}} = -\frac{\mathcal{G}}{\mathcal{G}^2+\alpha^2\mathcal{D}^2}\frac{\pi^2}{4}R_{\mathrm{h-skyr}}\gamma\beta J_{\mathrm{e}}$. This well explains the observed transverse motion of the endcap due to the spin current.

Accompanying the motion of the domain wall, magnetization rotates at magnetic domain walls due to the spin torque (Figs. 9(d) and 9(e)). This is consistent with recent experimental and theoretical results of current-induced variations of the effective DMI constant which alters both domain walls' motion and helicity [34]. Before applying the spin current, the left-handed Néel walls are stabilized by the DMI (Fig. 9(d)). In this configuration, there is a repulsive force between the two adjacent domain walls, since the energy of the system would increase with decreasing the distance between them (such as, with narrowing the $-M_{\mathrm{z}}$ domain in Fig. 9(d)). Applications of the spin current exert spin torques including the field-like torque and damping-like torque on magnetizations in the ferromagnetic layer. Spin torques behaving like the effective in-plane fields give rise to the reorientation of magnetizations (Fig. 9(e)), leading the repulsive force between adjacent domain walls to reverse into an attractive force. This results in the merging of $+M_{\mathrm{z}}$ domains, with the deletion of the topological defect (Fig. 9(c)).

In simulations, we have ignored the in-plane current flowing in the CoFeB layer. Micromagnetic simulations with only taking into calculations the in-plane current suggest that the spin-transfer torque due to the in-plane current does not induce obvious motion of the labyrinthine domain, and obvious changes in the orientational order of magnetic domain phases [23]. We have also not taken into consideration spatial variations of magnetic parameters that possibly lead to pinning sites of magnetic domains. Recent micromagnetic simulations studies show that grain boundaries have effects on skyrmion

motion [35,36]; however, one can still well qualitatively describe trajectories of the center of skyrmion mass through the Thiele equation. This leads us to believe that our micromagnetic simulation results yield a general picture for the response of magnetic domain walls to the spin torque.

Figure 9 only presents simulations results with applications of a small current. It has been shown in other simulations studies that the breaking of magnetic domains occurs when applying a large current [16,17]. The competition between the merging and breaking of magnetic domains results in the generation or deletion of topological defects, leading to the current-driven transition of the magnetic domain phase.

In a recent work from Zhang et al [24], authors nucleated skyrmions and observed the evolution of skyrmions into snake-like structures with decreasing the tilted magnetic field. The snake-like structures then transform into the oriented labyrinthine multi-domain that is aligned along the in-plane field. They have also observed the breaking of the labyrinthine domain into skyrmions with increasing the tilted magnetic field. The phenomena that the alignment of magnetic domains and the breaking of magnetic domains into skyrmions under an in-plane field, are similar to the spin torque effect observed in our work. In our studies, the labyrinthine domain is aligned perpendicular to the current and parallel to the spin polarization $\boldsymbol{m}_{\mathrm{p}}$ of the spin current. The effective field $\boldsymbol{H}_{\mathrm{FL}} \propto \boldsymbol{m}_{\mathrm{p}}$ caused by $\boldsymbol{\tau}_{\mathrm{FL}}$ behaves like an in-plane field, therefore causing similar manipulations of magnetic domain phases. This leads us to believe that our studies may give a hint on influences of topological defects on in-plane field-induced transitions of magnetic domain phases.

In summary, using P-MOKE microscope, we have observed spin torque-driven transitions of magnetic domain phases in a two-dimensional magnetic model system, in processes of which topological defects are demonstrated to be of significance. The labyrinthine domain phase supports multiple types of topological defects in a field-free environment. The topological defects can be deleted/generated by spin current with lower/higher current densities. Responses of topological defects to the spin current result in the change in the orientational order and domain width of the labyrinthine multi-domain at zero magnetic field. Since the resistance of a material depends on magnetic structures especially magnetic domain walls

[37], one can expect to employ current pulses to manipulate magnetic configurations and thus magnetic resistance. This may be potentially applied in future data storage and memory systems. The labyrinthine multi-domain can also be cut into dense skyrmions with applying a current pulse at a perpendicular magnetic field down to about 8.0 Oe. The great decrease in the magnetic field and the method of dynamically generation of skyrmions are essential for future skyrmion-based spintronic devices. A Thiele equation analysis and micromagnetic simulation study suggest that both the current-driven motion of topological defects and magnetization manipulations at domain walls are of significance in current-induced transitions. Our work provides a fundamental understanding of spin current-driven transitions of magnetic domain phases in a two-dimensional magnetic model system, which may also shed light on field-induced transitions in other quasi two-dimensional systems from one phase to another phase.

ACKNOWLEDGEMENTS

We acknowledge the financial support by the National Key R&D Program of China through Grant No. 2017YFA0303202 and by US National Science Foundation through Grants No. DMR-1307056.

REFERENCES:

[1] T. Meier, M. Kronseder, and C. Back, Phys. Rev. B **96**, 144408 (2017).
[2] N. Saratz, A. Lichtenberger, O. Portmann, U. Ramsperger, A. Vindigni, and D. Pescia, Phys. Rev. Lett. **104**, 077203 (2010).
[3] S. Woo *et al.*, Nat. Mater. **15**, 501 (2016).
[4] M. Yamanouchi, A. Jander, P. Dhagat, S. Ikeda, F. Matsukura, and H. Ohno, IEEE Magn. Lett. **2**, 3000304 (2011).
[5] G. Yu *et al.*, Nano Lett. **16**, 1981 (2016).
[6] M. Kronseder, T. Meier, M. Zimmermann, M. Buchner, M. Vogel, and C. Back, Nat. Commun. **6**, 6832 (2015).
[7] O. Portmann, A. Vaterlaus, and D. Pescia, Nature **422**, 701 (2003).
[8] N. Bergeard, J. Jamet, A. Mougin, J. Ferré, J. Gierak, E. Bourhis, and R. Stamps, Phys. Rev. B **86**, 094431 (2012).
[9] N. Abu-Libdeh and D. Venus, Phys. Rev. B **84**, 094428 (2011).
[10] A. Abanov, V. Kalatsky, V. L. Pokrovsky, and W. Saslow, Phys. Rev. B **51**, 1023 (1995).

[11] S. A. Kivelson, I. P. Bindloss, E. Fradkin, V. Oganesyan, J. Tranquada, A. Kapitulnik, and C. Howald, Rev. Mod. Phys. **75**, 1201 (2003).
[12] J. Sampaio, V. Cros, S. Rohart, A. Thiaville, and A. Fert, Nat. Nanotech. **8**, 839 (2013).
[13] X. Zhang, M. Ezawa, and Y. Zhou, Sci. Rep. **5**, 9400 (2015).
[14] R. Wiesendanger, Nat. Rev. Mater. **1**, 16044 (2016).
[15] K. Wang, L. Qian, S.-C. Ying, G. Xiao, and X. Wu, Nanoscale **11**, 6952 (2019).
[16] M. He *et al.*, Appl. Phys. Lett. **111**, 202403 (2017).
[17] S.-Z. Lin, Phys. Rev. B **94**, 020402 (2016).
[18] W. Chen, L. Qian, and G. Xiao, Sci. Rep. **8** (2018).
[19] A. Manchon, H. C. Koo, J. Nitta, S. Frolov, and R. Duine, Nat. Mater. **14**, 871 (2015).
[20] L. Liu, C.-F. Pai, Y. Li, H. Tseng, D. Ralph, and R. Buhrman, Science **336**, 555 (2012).
[21] Q. Hao and G. Xiao, Phys. Rev. B **91**, 224413 (2015).
[22] B. Dieny and M. Chshiev, Rev. Mod. Phys. **89**, 025008 (2017).
[23] See Supplementary Material at url. for details on determionation of magnetic skyrmions, quantification of the orientational order of magnetic domain patterns, and additional simulations.
[24] S. Zhang, J. Zhang, Y. Wen, E. M. Chudnovsky, and X. Zhang, Commun. Phys. **1**, 36 (2018).
[25] A. Thiele, Phys. Rev. Lett. **30**, 230 (1973).
[26] S. Seki and M. Mochizuki, *Skyrmions in magnetic materials* (Springer, 2016).
[27] A. Vansteenkiste, J. Leliaert, M. Dvornik, M. Helsen, F. Garcia-Sanchez, and B. Van Waeyenberge, AIP Adv. **4**, 107133 (2014).
[28] J. C. Slonczewski, J. Magn. Magn. Mater. **159**, L1 (1996).
[29] A. Conca, E. T. Papaioannou, S. Klingler, J. Greser, T. Sebastian, B. Leven, J. Lösch, and B. Hillebrands, Appl. Phys. Lett. **104**, 182407 (2014).
[30] J. Leliaert, J. Mulkers, J. De Clercq, A. Coene, M. Dvornik, and B. Van Waeyenberge, AIP Adv. **7**, 125010 (2017).
[31] T. Devolder *et al.*, Appl. Phys. Lett. **98**, 162502 (2011).
[32] R. Soucaille *et al.*, Phys. Rev. B **94**, 104431 (2016).
[33] J. Finley, C. H. Lee, P. Y. Huang, and L. Liu, Adv. Mater., 1805361 (2018).
[34] G. V. Karnad *et al.*, Phys. Rev. Lett. **121**, 147203 (2018).
[35] W. Legrand *et al.*, Nano Lett. **17**, 2703 (2017).
[36] J.-V. Kim and M.-W. Yoo, Appl. Phys. Lett. **110**, 132404 (2017).
[37] W. Chen, L. Qian, and G. Xiao, Phys. Rev. B **98**, 174402 (2018).